RSC Advances

This is an *Accepted Manuscript*, which has been through the Royal Society of Chemistry peer review process and has been accepted for publication.

Accepted Manuscripts are published online shortly after acceptance, before technical editing, formatting and proof reading. Using this free service, authors can make their results available to the community, in citable form, before we publish the edited article. This *Accepted Manuscript* will be replaced by the edited, formatted and paginated article as soon as this is available.

You can find more information about *Accepted Manuscripts* in the Information for Authors.

Please note that technical editing may introduce minor changes to the text and/or graphics, which may alter content. The journal's standard Terms & Conditions and the Ethical guidelines still apply. In no event shall the Royal Society of Chemistry be held responsible for any errors or omissions in this *Accepted Manuscript* or any consequences arising from the use of any information it contains.

ROYAL SOCIETY OF CHEMISTRY

www.rsc.org/advances

Effects of Transition Metal Precursors (Co, Fe, Cu, Mn, or Ni) on Pyrolyzed Carbon Supported Metal-aminopyrine Electrocatalysts for Oxygen Reduction Reaction

Pan Xu[a], Whenzhao Chen[a], Qiang Wang[b], Taishan Zhu[a], Mingjie Wu[a], Jinli Qiao,[a*] Zhongwei Chen,[c*], Jiujun Zhang[c]

[a]*College of Environmental Science and Engineering, Donghua University, 2999 Ren'min North Road, Shanghai 201620, P. R. China*

[b]*State Grid Shanghai Songjiang Electric Power Supply Company, 336, Ledu Rd., Songjiang Area, Shanghai 201600, P. R. China*

[c]*Department of Chemical Engineering,E6-2006, University of Waterloo, 200 University Avenue West, Waterloo, ON, N2L 3G1, Canada*

*Corresponding author. Tel: +86-21-67792379. Fax: +86-21-67792159. E-mail: qiaojl@dhu.edu.cn, zhwchen@uwaterloo.ca

Effects of Transition Metal Precursors (Co, Fe, Cu, Mn, or Ni) on Pyrolyzed

RSC Advances Accepted Manuscript

Carbon Supported Metal-aminopyrine Electrocatalysts for Oxygen Reduction Reaction

Pan Xu, Whenzhao Chen, Qiang Wang, Taishan Zhu, Mingjie Wu, Jinli Qiao, Zhongwei Chen, Jiujun Zhang

Abstract: In the past four decades, non-precious metal catalysts (NPMCs) have been extensively studied as low-cost catalyst alternatives to Pt for the oxygen reduction reaction (ORR) in polymer electrolyte membrane (PEM) fuel cells. However, the role of transition metal playing in the catalysts' active sites is still a subject of controversy. In order to further clarify the nature of the active sites of NPMCs, in this work, using aminopyrine (Apyr) as the nitrogen precursor, Co-, Fe-, Cu-, Mn-, and Ni-incorporated nitrogen-containing electrocatalysts are synthesized for fuel cell ORR in alkaline media. The catalysts' ORR performance can be significantly improved by pyrolysis when the catalysts are incorporated by different transition metals. The observed catalytic activity order is: Co >> Fe ~ Cu > Mn >> Ni. However, with respect to the electron transfer numbers (selectivity), the order is: Fe > Mn > Co >> Cu > Ni. XRD results reveal that Mn and Fe are more likely to be combined with S than Co, Ni and Cu. XPS analysis indicates that N concentration has a negative correlation with S concentration in the pyrolyzed catalysts, indicating a competitive mechanism between N and S on catalyst surfaces when metal sulfate is applied as the transition metal precursor. For ORR active site identification, the surface N species analysis reveals that catalyst containing more M-N group would give a higher catalytic ORR activity, while the metal incorporation is essential in the ORR active site structure, forming the M-N_x/C catalysts rather than just serving to catalyze the formation of N/C active sites.

Keywords: Transition metal precursor, active site, oxygen reduction reaction, polymer electrolyte membrane fuel cells.

1. Introduction

RSC Advances Accepted Manuscript

In the last several decades, polymer electrolyte membrane (PEM) fuel cells have evoked great interest from government agencies, academia and industry since it was first developed in the 1960's for space applications.[1,2] In a typical H_2/O_2 PEM fuel cell, hydrogen and oxygen react electrochemically at anode and cathode, respectively, producing electricity, heat and water. In this way, the chemical energy stored in hydrogen fuel can be directly and efficiently converted to electrical energy with water as the only byproduct, showing a great benefit to the effort of energy efficiency enhancement and environment protection.[3-5] Therefore, PEM fuel cell technology, together with various batteries and super capacitors have been recognized as the most promising devices for the next-generation of energy technologies, particularly for portable, stationary, and transportation applications.[6,7]

However, for commercialization, PEM fuel cells still face two major challenges, one is the high cost, and the other is the insufficient durability. Both of these two challenges are closely related to the electrocatalysts used for catalyzing cathode oxygen reduction reaction (ORR) and the anode hydrogen oxidation reaction (HOR). In particular, the ORR is the limited step in the overall PEM fuel cell reactions. This is because that the ORR at the cathode suffers from a sluggish ORR kinetics and a high over potential when compared to HOR at the anode. At the current state of technology, the most practical and effective electrocatalysts for ORR are Pt-based materials. Unfortunately, Pt material is both expensive and low abundance, which have been identified to be the major contributors to the challenges of high-cost of PEM fuel cells.[2,4,8] Furthermore, regarding the challenge of insufficient durability, there are two major contributing factors including (1) the cathode Pt catalyst is easily to be dissolved when the electrode is performed in a highly acidic environment and polarized at a positive potential,[9] and (2) Pt catalysts can be easily poisoned by the impurities in the feed system, resulting in performance degradation.[4,10,11] To overcome these challenges, developing alternative ORR electrocatalysts such as non-precious metal catalysts (NPMCs) have been becoming the most active approach in fuel cell catalyst research and development in the recent years. Although great efforts have

RSC Advances Accepted Manuscript

been made in this area, there have been still no major breakthroughs yet. Exploring alternative non-precious metal catalyst materials with both high ORR catalytic activity and sufficient stability is still an attractive research topic.[12-20]

Regarding NPMC ORR catalysts, several important kinds of unsupported or carbon supported materials have been developed in the past several decades, including unpyrolyzed and pyrolyzed transition metal nitrogen-containing complexes, conductive polymer-based catalysts, transition metal chalcogenides, metal oxides/carbides/nitrides/oxynitrides/carbonitrides, and enzymatic compounds. Among these candidates, pyrolyzed transition metal and nitrogen-containing complexes supported on carbon materials (M-N/C) are considered the most promising ORR catalysts.[21-27] Unfortunately, none of these NPMCs could be practically better than Pt-based catalysts in terms of both ORR activity and stability, in particular, the role of transition metal playing in the active sites of NPMCs is still a subject of controversy. Therefore, fundamentally understanding the performance mechanisms of NPMCs through both experimental and theoretical approaches is necessary. Up to now, there are two main different viewpoints on the role of transition metal playing in the catalysts. In most publications, the ORR active sites have been considered to be the M-N_x moieties,[21,23,28] where Fe (e.g., Fe-N_2/Fe-N_4/Fe-N_{2+2})[29-32]and Co (e.g., Co-N_4)[33] are known as the most active transition metal-ion centers. While in some other publications,[15,24,34-36] instead of being a part of the active site structure, the presence of the metal-ion center serves only to facilitate the incorporation of nitrogen into the carbon matrix during the pyrolysis, that is, the ORR activity should be attributed to the nitrogen functional groups doped in the carbon matrix, ie., N_x-C centers. This opinion is partially supported by the fact that the doped nitrogen can induce the charge delocalization for adjacent carbon atoms due to its strong electron affinity. The carbon atoms thus show a slightly positive charge due to charge delocalization, which facilitates the break of oxygen molecules by bonding in the form of parallel diatomic adsorption mode onto the carbon atoms.[13,37,38] Although there is a disagreement regarding the active sites for ORR, there is a general agreement that four elements must exist in order to obtain an ORR active catalyst (carbon-supported NPMCs): (i)

RSC Advances Accepted Manuscript

carbon, (ii) nitrogen source, (iii) transition metal source, and (iv) high temperature pyrolysis.[15,39]

With respect to the effects of transition metals on the ORR activity of the catalyst, Fe and Co are the most commonly used precursor metal ions for catalyst synthesis, whereas the other transition metals adjacent to them in the chemical periodic table such as Mn, Ni and Cu are less investigated.[40-45] Although these metal ions based catalysts may have less catalytic ORR activities than those of Fe- and Co- based ones, a systematic investigation may help further understand the nature of active sites.

In this paper, with Mn, Fe, Co, Ni, and Cu in the form of their sulfate salts as the typical transition metal precursor targets, the effects of transition metal ions on their catalytic ORR activity have been studied. Aminopyrine (Apyr) with a high content of nitrogen and favorable combination of aromatic ring and nitrogen-containing groups, and Vulcan-BP2000 carbon particles with a surface area of ~1500 m^2 g^{-1}, were chosen as the nitrogen and carbon sources, respectively, for the catalyst synthesis. For studying the ORR kinetic parameters and possible reaction mechanisms, the electrocatalytic activities of synthesized M-Apyr/C catalysts are systematically evaluated by cyclic voltammetry (CV) and linear sweep voltammetry (LSV) using both rotating disk electrode (RDE) and rotating ring-disk electrode (RRDE) techniques in alkaline media. For fundamental understanding, XRD, TEM and XPS analyses were performed to determine the active sites of these pyrolyzed catalysts and their relations to the transition metals.

2. Experimental

2.1 Materials and catalyst preparation

For catalyst preparation, aminopyrine (Apyr) provided by Sinopharm Chemical Reagent Co., Ltd(chemical pure) was used as the nitrogen precursor. Vulcan-BP2000 carbon black was used as carbon support, provided by Carbot Corporation with a specific surface area of 1475 m^2g^{-1}. For a convenient discussion, all catalysts reported in this paper are designed as A, B, C, D, E, F and G, respectively. Catalysts C–G were

RSC Advances Accepted Manuscript

synthesized in a typical procedure as follows: a mixture of *w* grams of MSO_4xH_2O (M = Mn, Fe, Co, Ni, or Cu, *x*=1,7,7,6, or 5, and *w* is the weight of salt), 0.070g Apyr, and 0.120g BP2000 carbon black were mixed with 20 ml methanol, milled for about 1 hour in a mortar, and then vacuum dried at 60°C for 1 hour, enabling the complete evaporation of methanol. The obtained powder was further placed in a quartz boat and pyrolyzed at 700°C for 2 hours in a flowing nitrogen atmosphere to obtain the final catalyst sample.

Catalyst A was prepared by mixing and drying *w* gram of $CoSO_47H_2O$, 0.070g Apyr and 0.120g BP2000 carbon black in the same way as that for Catalysts C-G described above, but without further process of pyrolysis. Catalyst B was also synthesized in the same way as that of Catalysts C–G but without the addition of transition metal precursor. For all the prepared catalysts, the initial total content of M (Mn, Fe, Co, Ni, Cu) was controlled to be about 5% according to Equation (1),where M_1 is atomic weight of M, M_2 is the molecular weight of transition metal precursor, *w* is the weight of transition metal precursor used in the synthesis process, *m* is the number of M atom in the transition metal salt precursor molecule, 0.120 is the weight of BP2000, and 0.070 is the weight of Apyr, respectively:

$$\frac{w\frac{mM_1}{M_2}}{0.120+0.070+w}=5\% \qquad (1)$$

A scheme of all preparations is shown in Fig. 1.

2.2 Electrochemical measurements

The electrocatalytic activities of Catalysts A–G were evaluated by cyclic voltammetry (CV) and linear sweep voltammetry (LSV) using both rotating disk electrode (RDE) and rotating ring-disk electrode (RRDE) techniques. A glassy carbon (GC) disk electrode with a diameter of ca. 6.0 mm (0.25 cm^2 geometric surface area) purchased from Pine Instruments was used as the working electrode. Before any measurement, the GC electrode surface was polished with Al_2O_3 (0.05μm) suspension

RSC Advances Accepted Manuscript

and rinsed with deionized water for several times. The catalyst ink was prepared by combining 4mg of the catalyst and 2ml of isopropyl alcohol, which was ultrasonically dispersed for 45 minutes to dissolve as evenly as possible. Then 10μL of the ink was deposited onto the GC electrode surface to form a uniform layer across the electrode surface. After drying at room temperature, 7μL of methanol/Nafion® solution (100:1 wt.%) was dropped onto the top of the catalyst layer to improve adhesion during the electrochemical measurement.

All measurements were carried out using a standard three-compartment electrochemical cell filled with 0.1M KOH electrolyte aqueous solution at room temperature. The GC electrode coated with catalyst was used as the working electrode. A saturated calomel electrode (SCE) was used as the reference electrode, and a platinum wire was used as the counter electrode. Measured potentials were converted to the values referred to a reversible hydrogen electrode (RHE). The cyclic voltammograms were performed by scanning the potential from 0.2 to 1.3V at a scan rate of 50 mV s^{-1} to measure the surface behavior of the catalyst in O_2-saturated 0.1M KOH solution. For LSV study, the potential range was between 0.2 and 1.0V in O_2-saturated 0.1M KOH solution. A slow scan rate of 5 mV s^{-1} was used to ensure a steady-state in each point of the curve. To verify the ORR catalytic pathway of the catalyst, the RRDE measurements were further performed to monitor the formation of peroxide species during the ORR process.

2.3 Physical characterizations

The crystal-phase X-ray diffraction (XRD) patterns of Catalysts A–G were obtained using a Philips PW3830 X-ray diffractometer equipped with Cu-Ka radiation (λ=0.15406 nm). The current was 40 mA and the voltage was 40 kV. The intensity data were collected at 25^{o}C in the 2θ range from 5^o to 90^o with a scan rate of 20^{o}min^{-1}. Transmission electron microscopy (TEM) analyses were performed with a high-resolution Hitachi JEM-2100F operating at 200 kV to obtain information of the average particle size and the distribution of the catalyst prepared. The X-ray photoelectron spectroscopy (XPS) was used to monitor the electrocatalyst surface or

RSC Advances Accepted Manuscript

subsurface composition, along with the chemical states of their surface catalyst particles. This measurement was carried out on a Kratos AXIS Ultra^{DLD} electron spectrometer with Al K X-ray anode source (hv=1486.6eV) at 250W and 14.0kV. All spectra were calibrated by setting the C 1s photoemission peak for sp^2-hybridized carbons to 284.8eV. The XPS Peak 41 software was used for fitting the XPS spectrum.

3. Results and discussion

3.1 Catalytic ORR activities of the catalysts

3.1.1 CV measurements

To study the effects of transition metal ions and nitrogen doping on ORR activity, Vulcan-BP2000 carbon black without heat-treatment was also used as a reference catalyst. Fig. 2 shows the cyclic voltammograms recorded using electrodes coated with Catalysts A–G and Vulcan-BP2000 at a loading of 81μgcm^{-2}, in O_2-saturated 0.1M KOH at room temperature. Clear oxygen reduction peaks can be observed for all of the catalyst samples, suggesting that all the catalysts as-prepared, even Vulcan-BP2000, are ORR active. However, peak positions of unpyrolyzed Catalyst A and metal-free Catalyst B are very close to the peak position of Vulcan-BP2000. This suggests that the synthesis processes for these two catalysts may not improve their catalytic activities, on the contrary, both the pyrolysis and the transition metal incorporation are necessary in ORR activity improvement. Then, by comparing the CVs of Catalyst A (unpyrolyzed Co-incorporated catalyst) and Catalyst E (pyrolyzed Co-incorporated catalyst), it is interesting to find that Catalyst E has a position peak at 0.784 V, which shows a 157mV more positive ORR peak potential (E_p) than Catalyst A (Table 1). Besides, the reduction peak current of Catalyst E (-1.6 m A cm^{-2}) is 60% higher than that of Catalyst A (-1.0 m A cm^{-2}), demonstrating that a pyrolysis process is indispensable for ORR activity improvement. This is consistent with the common belief that heat-treatment can effectively improve the ORR catalytic activity of catalysts.[26,27] In addition, by comparing the CVs of all metal-incorporated catalysts

RSC Advances Accepted Manuscript

(Catalysts C–G) with metal free Catalyst B, it can be clearly seen that catalyst C–G all exhibit much higher catalytic ORR activities than that of Catalyst B(metal-free Catalyst), indicated by their E_P values. Even for catalyst F (pyrolyzed Ni-incorporated catalyst), the lowest ORR activity indicated by its E_P value among the catalysts tested shows more than 30 mV positive shift than the metal-free one (Table 1). These results imply that metal-incorporation is also necessary for ORR activity improvement. In fact, the Catalysts C–G with different metals exhibited quite different catalytic ORR activities according to both their peak potential and the reduction peak current values, suggesting that catalytic activity is strongly dependent on the type of transition metal ions.

3.1.2 LSV measurements

For further studying the catalyst's ORR activity, linear sweep voltammetry (LSV) using rotating disk electrode (RDE) technique was performed. The obtained ORR polarization curves of Catalysts A–G at a catalyst loading of 81μgcm^{-2}in O_2-saturated 0.1M KOH at room temperature are presented in Fig. 3. As can be seen, the Catalyst E, ie., the pyrolyzed Co-incorporated catalyst, shows the highest ORR activity among all the catalysts in terms of both the onset potential (E_{onset}) and the half-wave potential ($\Delta E_{1/2}$), where the E_{onset} value and the $\Delta E_{1/2}$ value reach to 0.868 V and 0.800 V vs. RHE, respectively (Table 1). These values are 113 mV and 142 mV more positive than that of metal-free Catalyst B, demonstrating a significant enhancement in ORR activity after Co-incorporation.

To compare the ORR activity of the best performed catalyst (Catalyst E) in this paper with recently reported M-N/C catalysts, Table 2 shows the performance of Catalyst E and other M-N/C catalysts in terms of the ORR onset potential, half-wave potential and diffusion-limiting current. It can be seen that the onset potential of Catalyst E is slightly higher than that of Co10-NMCV,[46] while it is lower than the onset potentials of other three catalysts.[47-49] However, the half-wave potential of catalyst E is just lower than that of FePc/b-MWCNTs[48], but higher than other listed catalysts. Additionally, the diffusion-limiting current of catalyst E is the highest

RSC Advances Accepted Manuscript

among all. Note that the catalysts' performance was tasted at a very low catalyst loading (81μg/cm^2) in this paper, higher ORR activity could be obtained at higher loading.

It should be mentioned that catalysts C–G are incorporated by transition metals Mn, Fe, Co, Ni, and Cu but using the same anion sulfate precursor, therefore, the observed results should come from the contribution of incorporated transition metal ions. Given a further observation, one can see that the catalytic activities of these catalysts follow the order: E >> D ~ G > C >> F, that is, the order of catalytic ORR enhancement by transition metal incorporation should be: Co >> Fe ~ Cu > Mn >> Ni (Fig. 3 and Table 1). It is noted that the Co-incorporated catalyst gives a well-defined diffusion-limiting platform, suggesting that the ORR active sites of Co-incorporated catalyst might be evenly distributed on the catalyst surface. On the contrary, the Fe-incorporated one exhibits the poorest effect on diffusion-limiting platform, but the highest diffusion-limiting current among all the catalyst samples tested. In fact, the catalysts A–G give large differences in diffusion-limiting currents, which suggest that the ORR mechanisms catalyzed by these catalysts are evidently different, particularly in terms of the overall electron transfer number. This possibility will be confirmed further by the RRDE results in a later section.

3.1.3 RRDE measurements

In order to further confirm the overall or apparent electron transfer number for the catalyzed ORR, the RRDE technique was used to quantitatively detect the peroxide (H_2O_2) formed during the O_2 reduction process, and verify the ORR catalytic pathways. Based on the measurements of ring and disk currents, the apparent electron transfer number (n) and the hydrogen peroxide yield ($\%H_2O_2$) can be calculated based on the following equations[50]:

$$n = \frac{4I_d}{I_d + I_r / N} \qquad (2)$$

$$\%H_2O_2 = 100 \times \frac{2I_r / N}{I_d + I_r / N} \qquad (3)$$

RSC Advances Accepted Manuscript

Where I_d, I_r and N are the disk current, ring current and ring collection efficiency (0.37 in this work), respectively. Calculated $\%H_2O_2$ and n from the RRDE data are shown in Fig. 4 (a) and (b). In Table 1, the hydrogen peroxide yield and electron transfer number for Catalysts A–G are also compared, at a potential of 0.4V vs. RHE. From the comparison of Catalysts A and E, one can see that $\%H_2O_2$ is sharply dropped by 30% after pyrolysis and the electron transfer number is increased by 0.6. This result is well consistent with the observation in Fig. 2, further confirming the importance of pyrolysis.

To discuss the influence of different transition metal precursors, Catalysts C–G can be compared with metal-free Catalyst B. From Fig. 4, different metal ions can give very different percentages of H_2O_2 production, leading to different apparent ORR electron transfer numbers. Among all catalysts presented here, Fe-incorporated Catalyst D shows the lowest $\%H_2O_2$ values in the range of 4 – 13% (Fig. 4(a)) and the highest electron transfer numbers in the range of 3.7 – 3.9 over the potential range of 0.2 – 0.8V ((Fig. 4(b)). This may suggest that Fe-incorporated catalyst is an efficient choice for catalyzing ORR in a "direct" four-electron transfer reaction pathway. Regarding the most active Co-incorporated Catalyst E observed by both CV and LSV measurements, it also gives low $\%H_2O_2$ values in the range of 16–25% and high electron transfer numbers in the range of 3.5–3.7. To our interest, regarding Mn-incorporated Catalyst C, although it has a low performance observed by LSV measurement (Fig. 3), it shows quite low $\%H_2O_2$ values in the range of 13 – 22% and also high electron transfer numbers in the range of 3.55 – 3.75, which is even better than that of Co-incorporated Catalyst E. This phenomenon is similar to that of Fe-incorporated Catalyst D discussed above. In other words, the Fe- and Mn-incorporated catalysts both show high electron transfer numbers but low ORR activities. It seems that both the Fe- and Mn-incorporated catalysts possess intrinsic abilities to catalyze ORR in "direct" four-electron transfer reaction pathways. Since Fe and Mn are neighboring to each other in the chemical periodic table, it's reasonable to wonder that the ORR mechanisms catalyzed by these two catalysts are closely related to the nature of the transition metals.

RSC Advances Accepted Manuscript

For a better understanding, the data shown in Fig.4 (a) and (b) can be separated by the dash line, ie., catalysts under discussion can be roughly divided into two groups. As shown in Fig. 4 (b), the lower group includes Catalysts A, B, F and G, which are unpyrolyzed, metal free, Ni- and Cu-incorporated catalysts, respectively. The upper group includes Catalysts C, D and E, which are Mn-, Fe- and Co-incorporated catalysts, respectively. Apparently, the upper group catalysts, ie., the catalysts incorporated with Mn, Fe and Co, are more likely to catalyze ORR in "direct" four-electron transfer reaction pathways with much lower $\%H_2O_2$ yields than the lower group. With respect to the electron transfer numbers catalyzed by these metal-incorporated catalysts, the order is: Fe > Mn > Co >> Cu > Ni, which is interesting in accordance with the arrangement of these metals in the chemical periodic table.

For the rest two catalysts (Catalysts F and G), Ni-incorporated Catalyst F shows the highest $\%H_2O_2$ and lowest electron transfer number, and it also performs the worst ORR activities in both the CV and LSV measurements when compared to other metal-incorporated catalysts. In contrast, unlike Catalyst F, although Cu-incorporated Catalyst G also shows quite high $\%H_2O_2$ and low electron transfer number, it does not perform too poor ORR activities in the CV and LSV measurements. In fact, both the onset potential and half-wave potential for Cu-incorporated Catalyst G are even slightly higher than that for Fe-incorporated Catalyst E (Table 1). This may be due to the high nitrogen content doped in the catalyst, which will be discussed thoroughly in the later section of XPS analysis. It is noted that the diffusion limiting current of catalyst G is similar to that of catalysts C and E (Fig. 3), implying that the electron transfer number and $H_2O_2\%$ of these three catalysts should be almost the same. However, according to the RRDE results, $\%H_2O_2$ of catalyst G is much higher than that of catalysts C and E. This may be explained by the fact that although the active sites on Catalyst G could only catalyze ORR near the $2e^-$ transfer reaction pathway, the density of active sites can be high. The high density allows more O_2 to participate in ORR, thus the diffusion limiting current of Catalyst G can be comparable with that of Catalyst C and E. Another reason may be due to the fact that the pore structures in

RSC Advances Accepted Manuscript

those catalysts are different, and the intermediate product, ie. H_2O_2, produced by Catalyst G might be easier to be released into the electrolyte thus easier to be detected by the ring electrode. Different from Catalyst G, the H_2O_2 produced by Catalyst C and Catalyst E might be blocked in the micropores on the surface of the catalysts, thus the H_2O_2 production is less detected.

3.2 Morphology and structural characterization for ORR active site

3.2.1 X-ray diffraction results of the catalysts

As discussed above, transition metal incorporation can effectively influence the catalytic ORR activities of the catalysts in this work. However, what changes may occur on the catalyst surfaces after transition metal incorporation, and how do these changes influence the ORR activity are still unclear. Therefore, the influencing mechanisms of transition metal incorporation on the ORR activity need to be further studied. In this work, the X-ray diffraction (XRD) is first chosen to clarify the structure change after transition metals were incorporated. XRD patterns of Catalysts A – G are shown in Fig. 5. Two large broad peaks located at ca. 23.6° and 43.8°are due to the (002) and (100) reflection, which are commonly observed in amorphous carbon support BP2000[51] (Fig. 5(a)). These two peaks also exist in other XRD patterns because BP2000 carbon support is used for all other catalysts discussed here. For unpyrolyzed Catalyst A (Fig. 5(b)), the sharp peaks in the range of 20°–30° can be associated with the crystalline nature of aminopyrine, which are disappeared after pyrolysis, probably indicating aminopyrine is decomposed by the pyrolysis process. XRD patterns shown in Fig. 5(c) – (g) belong to the catalysts synthesized with various transition metals with pyrolysis process. Sharp diffraction peaks that can be clearly observed for all these catalysts suggest that metal crystal particles are present on the catalyst surfaces. In Fig. 5(c) for Mn-incorporated Catalyst C, the diffraction peaks at 29.6, 34.3, 49.3, 61.4, 72.3 and 82.5 correspond to the (110), (200), (220), (222), (400) and (420) crystalline planes of face-centered cubic crystalline Alabandite (Mn+2S), respectively (PDF 06-0518). Diffraction peaks at 29.9, 34.0, 44.0 and 53.7 in Fig. 5(d) for Fe-incorporated Catalyst D correspond to the (100), (101), (102) and (110)

RSC Advances Accepted Manuscript

crystalline planes of hexagonal Iron sulfide (FeS), respectively (FDF 65-9124). Unlike the sharp and narrow peaks in Fig. 5 (c), the diffraction peaks of iron sulfide related catalyst are lower and broader. These low and broad peaks imply that the crystal particles of iron sulfide related catalyst have a smaller size, which can be confirmed by the TEM images in the following section. The above XRD results indicate that the crystallographic Mn and Fe species are both in the form of combining with sulfur, without Mn or Fe simple substance presented.

For Co-incorporated Catalyst E (Fig. 5(e)), diffraction peaks can be observed at 15.4, 29.8, 31.2, 39.5, 47.6 and 52.1, corresponding to the (111), (311), (222), (331), (511) and (440) crystalline planes of face-centered cubic cobalt sulfide (Co_9S_8), respectively (PDF 65-6801). The other peak located at $2\theta = 44.2$ should be associated with the (111) crystalline plane of face-centered cubic Cobalt (PDF 15-0806). As revealed by the XRD pattern of Catalyst E, cobalt sulfide and cobalt simple substance co-exist on the catalyst surfaces.

In Fig. 5(f), diffraction peaks at 44.5, 51.8 and 76.3 correspond to the (111), (200) and (220) crystalline planes of face-centered cubic nickel, respectively (PDF 65-2865). And, other two diffraction peaks at 29.7 and 50.1 can be associated with the (111) and (220) crystalline planes of primitive cubic nickel sulfide (Ni_4S_3), respectively (PDF52-1027). In Fig. 5(g), diffraction peaks at 43.4, 50.6 and 74.3 correspond to the (111), (200) and (220) crystalline planes of face-centered cubic copper, respectively (PDF 65-9743). Other peaks at 31.5, 32.7, 39.1, 45.5, 46.1, 48.2, 53.7 and 66.6 are ascribed to the primitive tetragonal copper sulfide (Cu1.81S) (PDF 41-0959). As a result, the crystallographic Co, Ni and Cu also present in the form of simple substance besides their combination with sulfur, which are different from the results for Mn- and Fe-incorporated catalysts.

For a further understanding of the interactions between these metals and S in the catalyst, peak area and peak area ratios of the metallic crystal species obtained from XRD results are presented in Table 3. From Table 3, it can be seen that Mn-incorporated Catalyst C and Fe-incorporated Catalyst D both show high peak area of metal sulfide. On the contrary, the simple substance areas of both of them are zero,

RSC Advances Accepted Manuscript

which leads the ratios of M/M-S for Catalyst C and D are also to be zero. The peak area of Co indicates the appearance of Co simple substance on the surface of Catalyst E, and the ratio of M/M-S for catalyst E is calculated to be 0.38. For Catalysts F and G, the peak areas of simple substance are both much higher than that of metal sulfates, and the ratios of M/M-S are as high as 2.04 and 1.12, respectively. The high content of metallic Ni and Cu, which are not active for the ORR, may block the porosity of the catalysts. This may explain the fact that why we observed lower ORR activities for Catalyst F and G. Comparing the ratios of M/M-S for catalysts C, D, E , F and G, it is reasonable to give a conclude that Mn and Fe are more likely to be combined with S during the pyrolysis process, rather than form or help to form N-doped active sites. This assumption makes the lower ORR activity of Catalyst C and D than that of Catalyst E understandable, and will be confirmed in the XPS analysis.

3.2.2 Morphological analysis from TEM images

TEM images were acquired to get more precise structural information for our catalysts, as shown in Fig. 6. It can be seen that unpyrolyzed Catalyst A and metal free Catalyst B show similar morphologies (Fig. 6(a) and (b)) without observable decorating nanoparticle phase. These morphologies could be dominated by the morphology of BP2000. For example, the particles size is about 20nm, which is in accordance with the size of pristine BP2000 (15nm). Take a careful look at the high resolution TEM image of Catalyst B (inset, Fig. 6(b)), graphitic layers in the surface of the catalyst can be observed. The graphitic layers implies that the carbon support BP2000 and/or the nitrogen precursor aminopyrine have been slightly graphitized during the heat-treatment in N_2.

Fig. 6 (c) shows the TEM images of Mn-incorporated Catalyst C. A large block of metal crystal clusters can be observed on the catalyst surface. According to the XRD analysis, the crystal clusters should be Alabandite. These metal crystals are observed to grow in different directions (inset, Fig. 6(c)), indicating that it's a stack of several smaller metal crystal particles rather than a single one. Such a large scale of crystal stack observed can explain the sharp peak, which is the highest among all patterns, in

RSC Advances Accepted Manuscript

the XRD pattern of Catalyst C (Fig. 5(c)). The stacked particles reveal the aggregation of Mn on the surface of Catalyst C during the pyrolysis. Additionally, no carbon layer can be observed at the edge of these crystal particles, suggesting that Mn particles are not well combined to the carbon support, since they are not encased in the carbon shells. Fig.6 (d) shows the TEM images of Fe-incorporated Catalyst D. Unlike the aggregated large crystal particles in Fig.6 (c), particles in Fig.6 (d) are quite small, with a size of ca. 2 nm. These small particles can explain the low and broad diffraction peaks in Fig.5 (d). As pointed by the red arrow, there is a small area full of black dots, but no carbon support can be observed underneath. It seems that the particles are fallen off from the catalyst surface, probably indicating that the Fe particles are also not encased in carbon shells and, as a result, not well combined with the carbon support. The poor connection between Fe or Mn with carbon support should be another factor causing poor ORR performance of Catalyst C and Catalyst D compared to Catalyst E. Regarding Co-incorporated Catalysts E, the TEM images was presented in Fig. 6(e), where the particles can be seen evenly dispersed on the catalyst surfaces. Those particles are generally with sizes of 10-20 nm, and the crystal structures of them can also be observed in the high resolution image (inset, Fig. 6(e)). According to the XRD analysis, particles in Fig. 6 (e) could be either cobalt sulfide or cobalt simple substance. For Ni-incorporated Catalyst F as shown in the TEM images (Fig. 6 (f)), there is only one large metal crystal particle in the high resolution image (inset, Fig. 6 (f)), with a size of ca. 30nm. The Ni particle seems to be covered by very thin carbon layers. Very interestingly, in the lower resolution image, it is still the only metal crystal particle that can be seen, showing that Ni is also quite aggregated on the catalyst surfaces. The TEM images shown in Fig. 6 (g) is for Cu-incorporated catalyst G, in which two metal particles with sizes of ca. 20nm can be observed. The high resolution image shows a better vision (inset, Fig. 6 (g)), in which metallic crystal structure can also be observed. Unlike the exposed Fe and Mn particles, this Cu particle is clearly observed to be encased in carbon shells, indicating it's well combination with the carbon support.

RSC Advances Accepted Manuscript

3.2.3 XPS analysis and active sites for the ORR

To study the surface species of the catalysts, X-ray photoelectron spectroscopy analysis was carried out. Elemental compositions detected with XPS are summarized in Table 4. As an aforementioned assumption in XRD analysis, Mn and Fe are more likely to be combined with sulfur during the pyrolysis. This assumption can be further confirmed by the sulfur concentration of each metal sulfate incorporated catalyst in Table 4, which gives the order of Fe > Mn > Co > Cu > Ni. It was noted here that the nitrogen concentrations on Catalysts F and G are apparently higher than that of Catalysts C, D and E. This may implies that the nitrogen concentration shows a negative correlation with the sulfur concentration. This negative correlation suggests that there is a competitive mechanism between nitrogen (N) and sulfur (S) for metal during pyrolysis. Namely, if more metal ions are combined with S, there remains less to combine with N. Considering that M-N_x moieties are more ORR active than M-S_y ones, low ORR activities of both Fe- and Mn-incorporated catalysts are caused by their week combination with N or strong combination with S which is in accordance with the LSV results as we observed in Fig. 3. According to the literatures,[43,52,53] ORR has a positive correlation with N content. However, it should be noted that since different species of metal are applied in this work, the correlation between ORR activity and N content seems not that simple. In other words, the ORR activity doesn't show linear relationship with the N concentration as can be seen in Table 4.

Fig. 7 (a)–(g) present the N1s spectra of Catalysts A–G, respectively. Regarding N-groups, Pels *et al.*[54] systemically studied the nitrogen functional groups in coals and chars, and reported that during the carbon decomposition at temperature higher than 600^{o}C, two major nitrogen functional groups can be formed on the carbon substrate, which were quaternary-N and pyridinic-N. Although these two nitrogen species were quite stable at high temperatures, some additional nitrogen functional groups were also possible on carbon. In this work, the N1s spectrum is de-convoluted into four peaks which are pyridinic-N (398.7eV), pyrrolic-N (399.8eV), quaternary-N (401.1eV) and oxidized-N (402-405eV),[54-57] respectively.

For a better comparison, the N1s spectrum of unpyrolyzed Catalyst A is also

RSC Advances Accepted Manuscript

de-convoluted in accordance with the four species, although there could be a wide variety of N species on the sample surface. From the XPS spectra comparison of Catalyst A (Fig. 7(a)) and Catalyst E (Fig.7(e)) that both are Co-incorporated catalysts but without and with pyrolysis treatment, respectively, a conspicuous transition can be observed after pyrolysis. For Catalyst A, only two peaks are observed which are ascribed to quaternary-N (401.1eV) and pyrrolic-N (399.8eV), respectively. However, for Catalyst E, there appear two additional peaks, of which the small one at 404 eV can be assigned to oxidized-N and the large one at 398.7eV can be assigned to pyridinic-N. Oxidized-N is believed to be formed after the sample is exposed to air [54,58] and gives no contribution to catalytic ORR activity, while pyridinic-N plays a key role in catalytic activity.[59,60] If associating the remarkable ORR activity of Catalyst E with the observed large pyridinic-N peak, one may propose pyridinic-N as the active site for ORR. However, the N1s spectrum of metal-free Catalyst B (Fig.8 (b)), which shows similar catalytic ORR activity to unpyrolyzed Catalyst A, also gives a conspicuous pyridinic-N peak. This may lead to a controversy that pyridinic-N is of no significance to ORR activity. Or, there is another possibility that pyridinic-N is of some significance, but it just acts as a part of the active site rather than being the only or dominating one. Based on previous analysis, two assumptions maybe made: (1) pyridinic-N may not take part in ORR catalysis process; and (2) pyridinic-N is a portion of the ORR active site, some other portion is also necessary. To clarify this point, other pyrolyzed catalysts can be compared. It can be seen that large pyridinic-N peaks can be observed to present in the XPS spectra of all catalyst samples, ie., Fig. 7 (c) for Mn-incorporated Catalyst C, Fig. 7 (d) for Fe-incorporated Catalyst D, Fig. 7 (f) for Ni-incorporated Catalyst F and, Fig. 7 (g) for Cu-incorporated Catalyst G, respectively. In particular, the emerging of pyridinic-N peak is the only conspicuous transition after pyrolysis in the N1s spectrum. This strongly proposes the later assumption (2) to be the fact. In other words, pyridinic-N is indeed a portion of the active site, but still another portion is needed to form a completed ORR active site.

For a more convenient comparison, the portions of each N species are summarized in Table 5. As can be seen from Table 5, pyridinic-N portion of Catalyst B (31.1%) is

RSC Advances Accepted Manuscript

close to that of Catalyst E (38.6%). This suggests that a large amount of pyridinic-N structure can be formed after pyrolysis even without metal incorporation. However, metal-free Catalyst B shows a much lower ORR activity than Catalyst E, implying that metal incorporation is essential in the ORR active site structure rather than just serving to catalyze the formation of N/C active sites during the pyrolysis procedure. So far, a conclusion should be made, that the ORR active site is formed by both transition metal and pyridinic-N. Namely, M-N_x center, which is bonded into carbon matrix to form the M-N_x/C catalyst, should be the ORR active site. This conclusion is in a well agreement with the work of Dodelet's group and other researchers.[14,16-19,28-33] In addition, in reference to the catalysts incorporated by other transition metals, Catalysts C, D, F, and G show variable pyridinic-N concentration in the range of 33.2 –40.9%. Regardless of their higher or lower surface pyridinic-N contents than Catalyst E, their ORR activities are generally lower. This further demonstrates that transition metal is a crucial role in the active site and also a decisive factor for the ORR activity. Furthermore, the even distribution of Co particles may indicate the even distribution of Co-N_x centers, facilitating high ORR activities and resulting well defined diffusion-limiting currents for Co-incorporated catalyst.

In literatures, quaternary-N has also been reported to be the active site for ORR.[61,62] However, since nitrogen in quaternary-N is located in the graphite plane and bonded to three carbon atoms, it is unlikely for quaternary-N to have more space for transition metals to form M-N_x/C structure. As discussed above, transition metal is the necessary portion of the catalyst ORR active sites, however, it is hard to agree with that the metal-free quaternary-N is the ORR active site. Additionally, it is noted that Catalysts B–G in this work show quite differing ORR activities, but the contents of quaternary-N portion in these catalysts are at the almost same level if the fluctuations are considered. Therefore, quaternary-N may also be unlikely to act as the active site, and thus not the group responsible for the catalytic ORR activity.

4. Conclusions

RSC Advances Accepted Manuscript

Using aminopyrine as nitrogen precursor, a metal-free catalyst and catalysts incorporated with several different transition metal precursors were synthesized. Through electrochemical measurements and physical characterization analysis, several observations/conclusions can be drawn as follows:

(1) As observed by both CV and LSV measurements, the catalyst without pyrolysis but containing metal ion (i.e., Co-incorporated) and the pyrolyzed metal-free catalyst show no difference in ORR activity improvement compared to pristine carbon black BP2000. However, the catalysts' ORR performance can be significantly improved by the pyrolysis when the catalysts are incorporated by different transition metals and follow the order of Co >> Fe > Cu > Mn >> Ni;

(2) As revealed by the RRDE measurements, the selectivity for ORR catalyzed by the catalysts follow the order of Fe > Mn > Co >> Cu > Ni. Fe-incorporated catalyst shows the lowest H_2O_2 yield and highest electron transfer number even though it has a relatively lower ORR activity, suggesting that this catalyst has an intrinsic ability to catalyze ORR in a "direct" four-electron transfer reaction pathway. The best performed Co-incorporated catalyst also shows a low H_2O_2 production (9–17%) and a high four-electron transfer selectivity, ie., n = 3.6 - 3.8;

(3) From XRD and TEM results, metallic crystal structures have been proven to be present on the metal-incorporated catalyst surfaces after pyrolysis. Those metallic crystal structures are either simple substance or sulfur combined metal, depending on the type of transition metal species. Fe and Mn are totally combined with S during the pyrolysis, whereas Co, Cu and Ni tend to form more metallic simple substances along with their combination with S;

(4) XPS analysis indicates that N concentration has a negative correlation with S concentration in the pyrolyzed catalyst samples, that is, the higher the S concentration in the catalyst, the lower the N concentration would be. When N concentration is higher, the formed M-N_x groups would be more, and the formed M-S_y group would be less. The catalyst containing more M-N_x group would give a higher catalytic ORR activity. This observation can explain the poor performance of Fe- and Mn-incorporated catalysts in which more metal ions are combined with S;

RSC Advances Accepted Manuscript

(5) Surface N species analysis reveals that both the carbon bonded pyridinic-N and metal are necessary in order to compose a catalytic ORR active site. In other words, a catalytic ORR active site is composed of carbon-bonded pyridinic-N and metal to form M-N_x/C catalyst.

So far, if all observations/conclusions above are referenced, two dominant factors should be concluded to decide the ORR activity. One is the intrinsic catalytic abilities of the M-N_x active site centers, following the order: Fe-N_x > Mn-N_x > Co-N_x >> Cu-N_x > Ni-N_x, indicated by RRDE results. While the favorable combination of Fe/Mn with S lead to the low content of Fe-N_x/Mn-N_x centers, thus the decreased catalytic ORR activity of Fe-Apyr/C and Mn-Apyr/C catalysts. The other major factor which decides the ORR activity is the density/content of M-N_x active site centers. The combined effect of these two factors leads to the activity order: Co-Apyr/C >> Fe-Apyr/C ~ Cu-Apyr/C > Mn-Apyr/C >> Ni-Apyr/C, indicated by CV and LSV results.

Acknowledgement

This work was supported by the National Natural Science Foundation of China (21173039); Specialized Research Fund for the Doctoral Program of Higher Education, SRFD (20110075110001) of China; International Academic Cooperation and Exchange Program of Shanghai Science and Technology Committee (14520721900) and the State Grid Shanghai Songjiang Electric Power Supply Company. All the financial supports are gratefully acknowledged.

References

1. H. Wang, M. A. Sweikart, J. A. Turner, *J. Power Sources*, 2003, **115**, 243-251.

RSC Advances Accepted Manuscript

2. Y. Wang, K. S. Chen, J. Mishler, S. C. Cho and X. C. Adroher, *Appl. Energy*, 2011, **88**, 981-1007.

3. D. Chu and R. Jiang, *J. Power Sources*, 1999, **83**, 128-133.

4. L. Zhang, J. Zhang, D. P. Wilkinson and H. Wang, *J. Power Sources*, 2006, **156**, 171-182.

5. S. Yerramalla, A. Davari, A. Feliachi and T. Biswas, *J. Power Sources*, 2003, **124**, 104-113.

6. P. L. Hentall, J.B. Lakeman, G. O. Mepsted, P. L. Adcock and J. M. Moore, *J. Power Sources*, 1999, **80**, 235-241.

7. L. Xiao, H. Zhang, T. Jana, E. Scanlon, R. Chen, E. W. Choe, L. S. Ramanathan, S.Yu and B.C. Benicewicz, *Fuel Cells*, 2005, **5**, 287-295.

8. Y. Ou, H. Kumagai, F. Yin, S. Okada, H. Hatasawa, H. Morioka, K. Takanabe, J. Kubota and K. Domen, *J. Electrochem. Soc.*, 2011, **158**, B1491-B1498.

9. P. J. Ferreira, G. J. la O', Y. Shao-Horn, D. Morgan, R. Makharia, S. Kocha and H. A. Gasteiger, *J. Electrochem. Soc.*, 2005, **152**, A2256-A2271.

10. M. Bron, J. Radnik, M. F. Erdmann, P. Bogdanoff and S. Fiechter, *J. Electroanal. Chem.*, 2002, **535**, 113-119.

11. X. Zhou, B. Hu, Z. Chen, F. Delgado and R. Srivastava, *Electrochem. Solid-State Lett.*, 2005, **8**, A616-A618.

12. J. Qiao, L. Xu, L. Ding, L. Zhang, R. Baker, X. Dai and J. Zhang, *Appl. Catal. B: Environ.*, 2012, **125**, 197-205.

13. Y. Zheng, Y. Jiao, J. Chen, J. Liu, J. Liang, A. Du, W. Zhang, Z. Zhu, S. C. Smith, M. Jaroniec, G. Q. Lu and S. Z. Qiao, *J. Am. Chem. Soc*., 2011, **133**, 20116-20119.

14. S. Gupta, D. Ttyk, I. Bae, W. Aldred and E. Yeager, *J. Appl. Electrochem.*, 1989, **19**, 19-27.

15. X. Li, G. Liu and B. N. Popov, *J. Power Sources*, 2010, **195**, 6373-6378.

16. M. Lefevre, E. Proietti, F. Jaouen and J. P. Dodelet, *Science*, 2009, **324**, 71-74.

17. M. Lefevre and J. P. Dodelet, *Electrochim. Acta*, 2008, **53**, 8269-8276.

18. R. Bashyam and P. Zelenay, *Nature*, 2006, **443**, 63-66.

19. G. Wu, K. L. More, C. M. Johnston and P. Zelenay, *Science*, 2011, **332**, 443-447.

RSC Advances Accepted Manuscript

20. Y. Zheng, Y. Jiao, L. Ge, M. Jaroniec and S. Z. Qiao, *Angew. Chem. Int. Ed.*, 2013, **52**, 3110-3116.

21. W. Li, J. Wu, D.C. Higgins, J.Y. Choi, Z.W. Chen, *ACS Catal.* 2012, **2**, 2761-2768.

22. Y. Hu, J. O. Jensen, W. Zhang, L. N. Cleemann, W. Xing, N. J. Bjerrum and Q. Li, *Angew. Chem. Int. Ed.*, 2014, **53**, 3675-3679.

23. A. Serov, M.H. Robson, K. Artyushkova and P. Atanassov, *Appl. Catal. B: Environ.*, 2012, **127**, 300-306.

24. M. Chokai, M. Taniguchi, S. Moriya, K. Matsubayashi, T. Shinoda, Y. Nabae, S. Kuroki, T. Hayakawa, M. Kakimoto, J. Ozaki and S. Miyata, *J. Power Sources*, 2010, **195**, 5947-5951.

25. J. Qiao, L. Xu, Y. Liu, P. Xu, J. Shi, S. Liu and B. Tian, *Electrochim. Acta*, 2013, **96**, 298-305.

26. Z. Chen, D. Higgins, A. Yu, L. Zhang and J. Zhang, *Energy Environ. Sci.*, 2011, **4**, 3167-3192.

27. C. W. B. Bezerra, L. Zhang, K. Lee, H. Liu, A. L. B. Marques, E. P. Marques, H. Wang and J. Zhang, *Electrochim. Acta*, 2008, **53**, 4937-4951.

28. S. L. Gojkovic, S. Gupta and R. F. Savinell, *J. Electroanal. Chem.*, 1999, **462**, 63-72.

29. G. Faubert, R. Cote, J. P. Dodelet, M. Lefevre and P. Bertrand, *Electrochim. Acta*, 1999, **44**, 2589-2603.

30. M. Lefevre, J. P. Dodelet and P. Bertrand, *J. Phys. Chem. B*, 2000, **104**, 11238-11247.

31. F. Charreteur, F. Jaouen, S. Ruggeri and J. P. Dodelet, *Electrochim. Acta*, 2008, **53**, 2925-2938.

32. C. E. Szakacs, M. Lefevre, U. I. Kramm, J. P. Dodelet and F. Vidal, *Phys. Chem. Chem. Phys.*, 2014, **104**, 11238-11247.

33. M. Lefevre, J. P. Dodelet and P. Bertrand, *J. Phys. Chem. B*, 2005, **109**, 16718-16724.

34. P. H. Matter and U. S. Ozkan, *Catal. Lett.*, 2006, **109**, 115-123.

RSC Advances Accepted Manuscript

35. S. Maldonado and K. J. Stevenson, *J. Phys. Chem. B*, 2005, **109**, 4707-4716.

36. P. H. Matter, E. Wang, J. M. Millet and U. S. Ozkan, *J. Phys. Chem. C*, 2007, **111**, 1444-1450.

37. R. Liu, D. Wu, X. Feng and K. Müllen, *Angew. Chem. Int. Ed.*, 2010, **49**, 2565-2569.

38. K. Gong, F. Du, Z. Xia, M. Durstock, L. Dai, *Science*, 2009, **323**, 760-764.

39. G. Liu, X. Li, P. Ganesan and B. N. Popov, *Appl. Catal. B: Environ.*, 2009, **93**, 156-165.

40. H. Zhang, Q. Jiang, L. Sun, X. Yuan, Z. Shao and Z. Ma, *Int. J. Hydrogen Energy*, 2010, **35**, 8295-8302.

41. I. Roche, E. Chaınet, M. Chatenet, and J. Vondrak, *J. Phys. Chem. C*, 2007, **111**, 1434-1443.

42. F. R. Brushett, M. S. Thorum, N. S. Lioutas, M. S. Naughton, C. Tornow, H. M. Jhong, A. A. Gewirth and P. J. A. Kenis, *J. Am. Chem. Soc*.. 2010, **132**, 12185-12187.

43. J. Ozaki, S. Tanifuji, A. Furuichi and K. Yabutsuka, *Electrochim. Acta*, 2010, **55**, 1864-1871.

44. L. Ding, J. Qiao, X. Dai, J. Zhang, J. Zhang and B. Tian, *Int. J. Hydrogen Energy*, 2012, **37**, 14103-14113.

45. L. Ding, X. Dai, R. Lin, H. Wang and J. Qiao, *J. Electrochem. Soc.*, 2012, **159**, F577-F584.

46. M. Li, X. Bo, Y. Zhang, C. Han, A. Nsabimana and L. Guo, *J. Mater. Chem. A*, 2014, **2**, 11672-11682.

47. Y. Ma, H. Wang, H. Feng, S. Ji , X. Mao and R. Wang, *Electrochim. Acta*, 2014, **142**, 317-323.

48. A. Morozan, S. Campidelli, A. Filoramo, B. Jousselme and S. Palacin, *Carbon*, 2011, **49**, 4839- 4847.

49. Z. Mo, S. Liao, Y. Zheng and Z. Fu, *Carbon*, 2012, **50**, 2620-2627.

50. M. Lefevre and J. P. Dodelet, *Electrochim. Acta*, 2003, **48**, 2749-2760.

51. J. Wang, G. Yin, Y. Shao, S. Zhang, Z. Wang, Y. Gao, *J. Power Sources*, 2007, **171**, 331–339.

RSC Advances Accepted Manuscript

52. F. Jaouen, S. Marcotte, J. P. Dodelet and G. Lindbergh, *J. Phys. Chem. B*, 2003, **107**, 1376-1386.

53. V. Nallathambi, N. Leonard, R. Kothandaraman and S. C. Barton, *Electrochem. Solid-State Lett.*, 2011, **14**, B55-B58.

54. J. R. Pels, F. Kaptuijn, J. A. Moulijn, Q. Zhu and K. M. Thomas, *Carbon*, 1995, **33**, 1641-1653.

55. T. S. Olson, S. Pylypenko, P. Atanassov, K. Asazawa, K. Yamada and Hirohisa Tanaka, *J. Phys. Chem. C*, 2010, **114**, 5049-5059.

56. P. Matter, L. Zhang and U. Ozkan, *Journal of Catalysis*, 2006, **239**, 83-96.

57. D. C. Higgins, J. Wu, W. Li and Z. Chen, *Electrochim. Acta*, 2012, **59**, 8-13.

58. K. Stanczyk, R. Dziembaj, Z. Piwowarska and S. Witkowski, *Carbon*, 1995, **33**, 1383-1392.

59. C. V. Rao, C. R. Cabrera and Y. Ishikawa, *J. Phys. Chem. Lett.*, 2010, **1**, 2622-2627.

60. Z. Chen, D. Higgins, H. Tao, R. S. Hsu and Z. Chen, *J. Phys. Chem. C*, 2009, **113**, 21008-21013.

61. N. P. Subramanian, X. Li, V. Nallathambi, S. P. Kumaraguru, H. Colon-Mercado, G. Wu, J.-W. Lee and B. N. Popov, *J. Power Sources*, 2009, **188**, 38-44.

62. G. Liu, X. Li, P. Ganesan and B. N. Popov, *Electrochim. Acta*, 2010, **55**, 2853-2858.

Figure captions

Fig. 1 Scheme of catalyst synthesis process

RSC Advances Accepted Manuscript

Fig. 2 Cyclic voltammograms of Catalysts A–G and pristine BP2000 in O_2-saturated 0.1M KOH solution at the ambient temperature. Scan rate: 50mV/s, catalyst loading: 81μg/cm^2.

Fig. 3 RDE polarization curves of ORR on Catalysts A–G in O_2-saturated 0.1M KOH solution at the ambient temperature. Scan rate: 5mV/s, electrode rotation rate: 1600rpm, catalyst loading: 81μg/cm^2.

Fig. 4 Calculated values of the ORR apparent electron transfer number (*n*) and $\%H_2O_2$ during ORR catalyzed by Catalysts A – G.

Fig. 5 XRD patterns of Catalysts (a) B, (b) A, (c) C, (d) D, (e) E, (f) F and (g) G.

Fig. 6 TEM images of Catalysts (a) A, (b) B, (c) C, (d) D, (e) E, (f) F and (g) G.

Fig. 7 XPS-N 1s data of Catalyst (a) A, (b) B, (c) C, (d) D, (e) E, (f) F and (g) G. The red, green, blue and magenta lines correspond for oxidized-N, quaternary-N, pyrrolic-N and pyridinic-N, respectively.

RSC Advances Accepted Manuscript

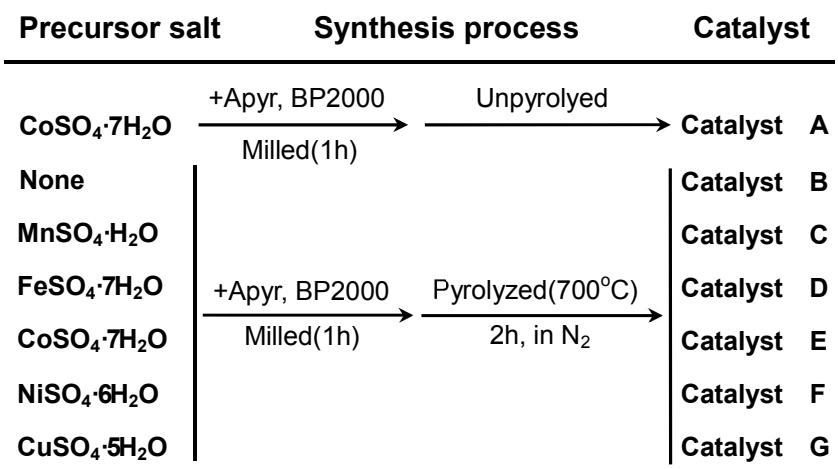

Fig. 1

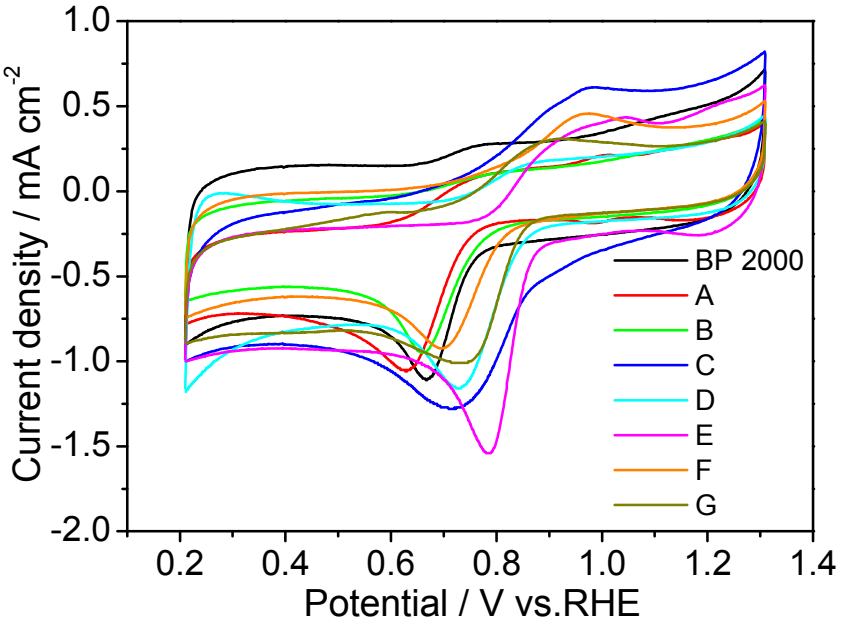

Fig. 2

RSC Advances Accepted Manuscript

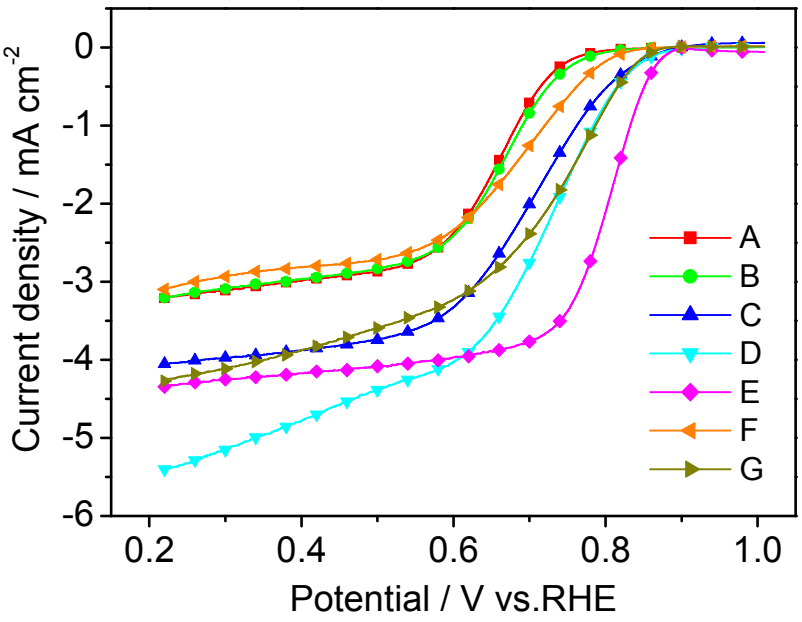

Fig. 3

RSC Advances Accepted Manuscript

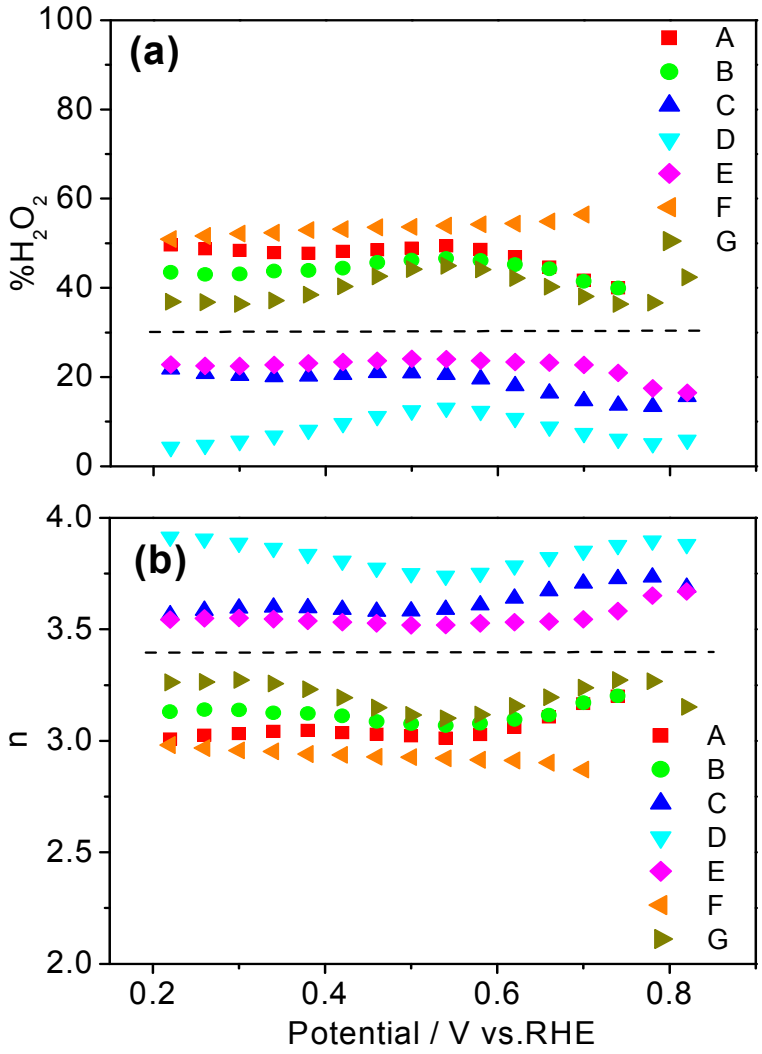

Fig. 4

RSC Advances Accepted Manuscript

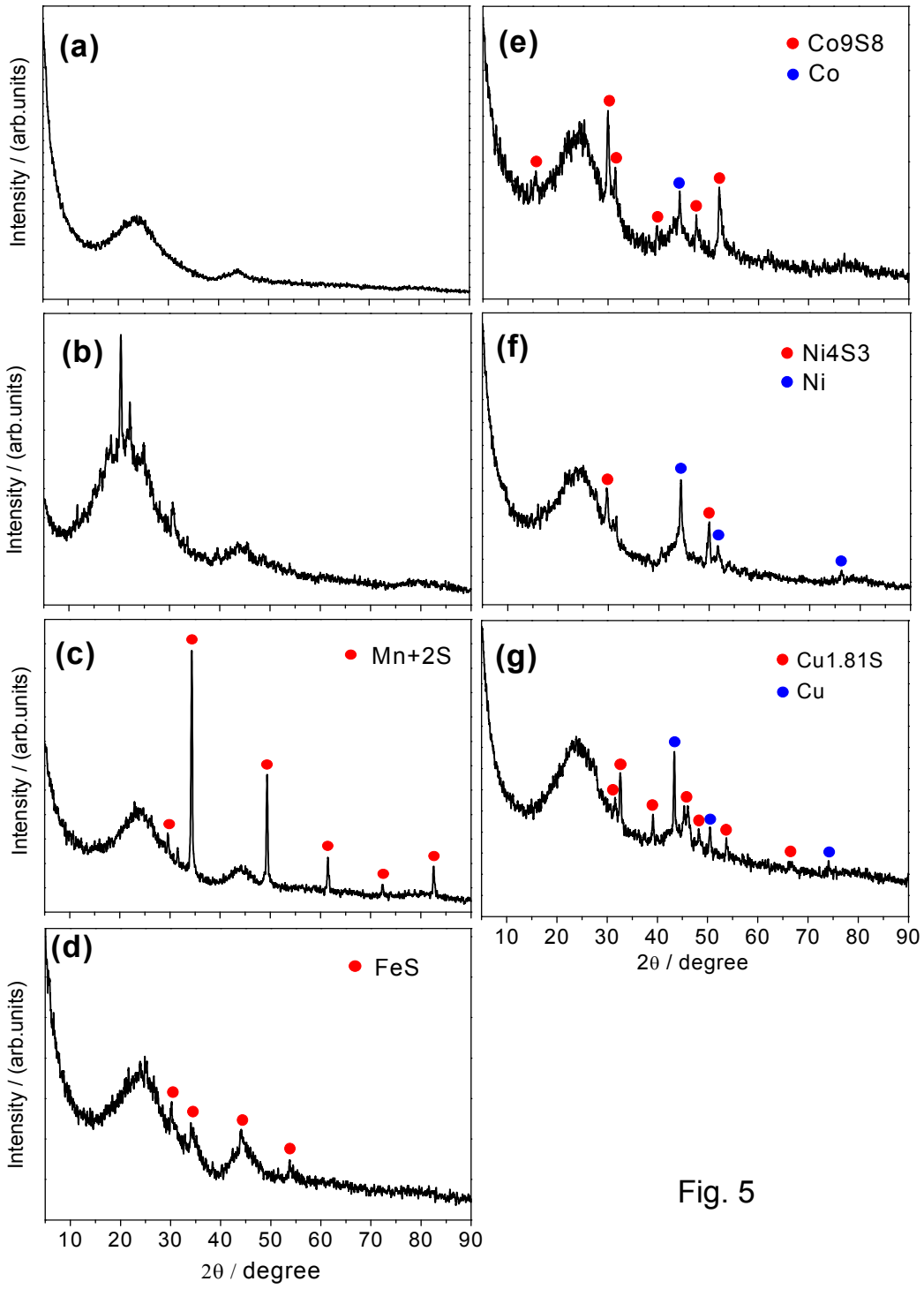

Fig. 5

RSC Advances Accepted Manuscript

RSC Advances Accepted Manuscript

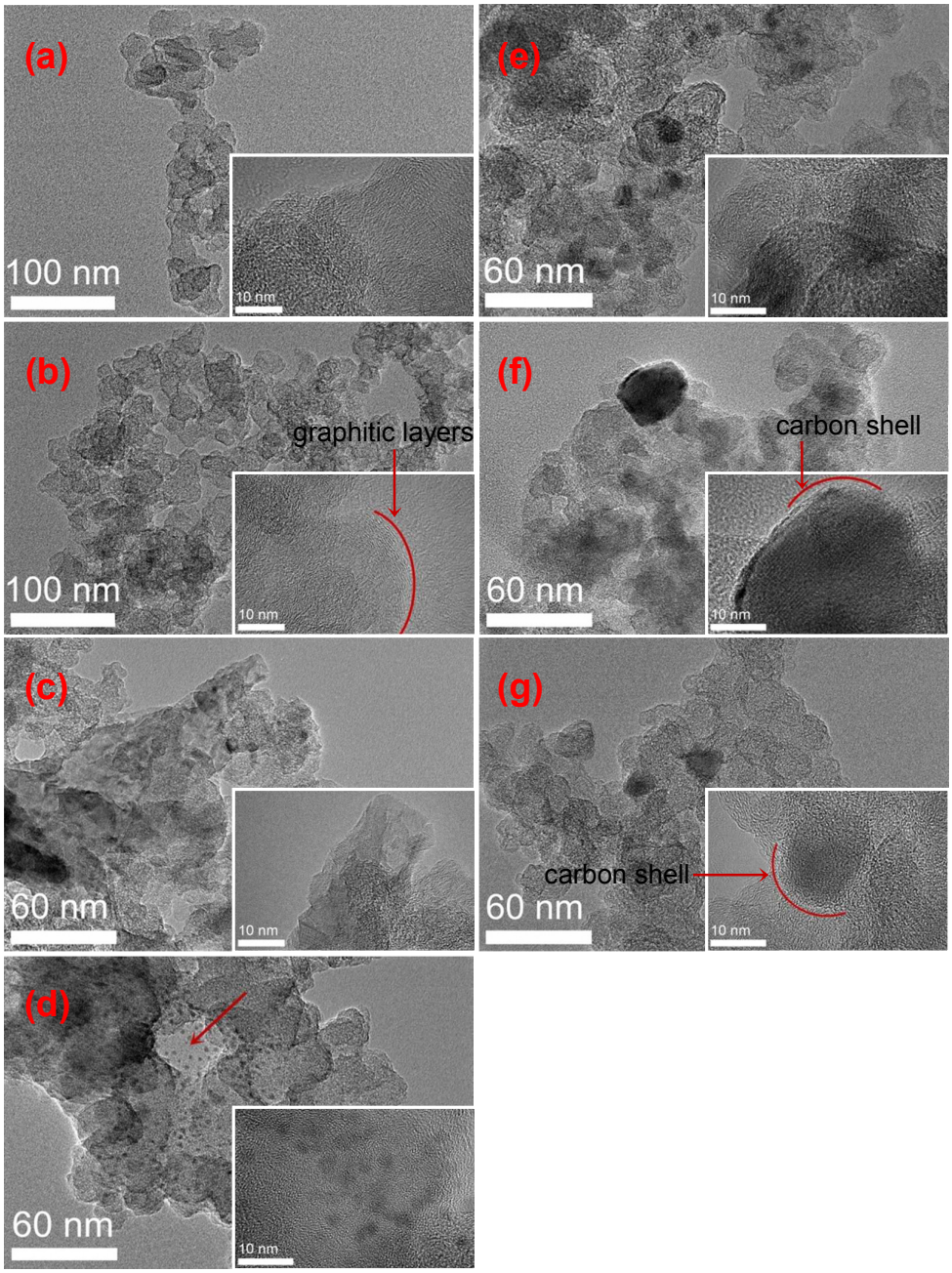

Fig. 6

RSC Advances Accepted Manuscript

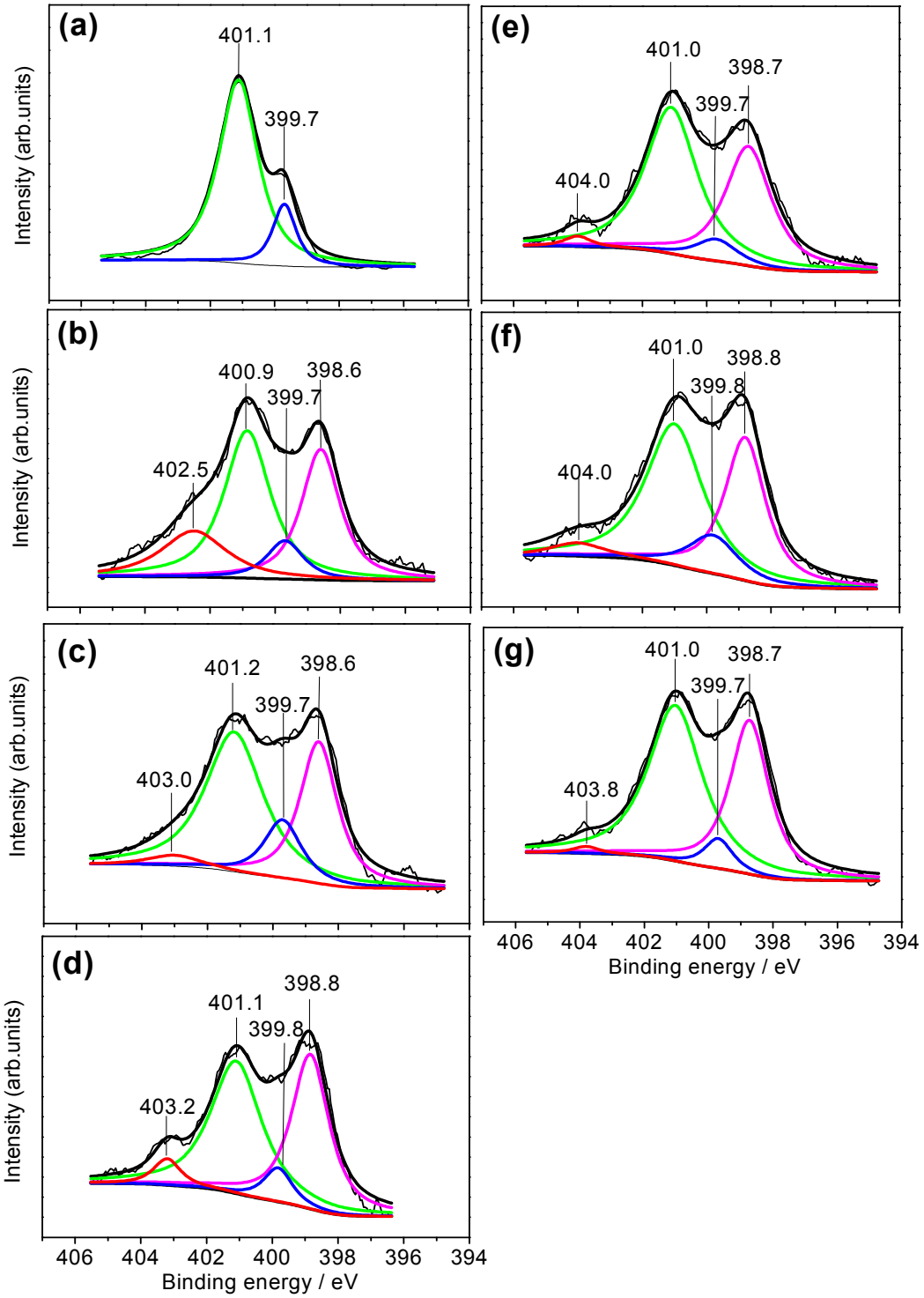

Fig. 7

Table 1 Kinetic parameters for catalyst A –G.

RSC Advances Accepted Manuscript

Catalyst[a]	Metal precursor	E_P/V	E_{onset}/V	$\Delta E_{1/2}$/ V	j at 0.4V (mA/cm^2)	%H_2O_2 at 0.4V	n at 0.4V
A	$CoSO_4$	0.627	0.757	0.658	-2.87	49	3.0
B	/	0.660	0.771	0.665	-2.83	46	3.1
C	$MnSO_4$	0.716	0.844	0.705	-3.74	21	3.6
D	$FeSO_4$	0.729	0.841	0.721	-4.38	12	3.8
E	$CoSO_4$	0.784	0.868	0.807	-4.08	24	3.5
F	$NiSO_4$	0.694	0.807	0.688	-2.72	54	2.9
G	$CuSO_4$	0.730	0.842	0.735	-3.59	44	3.1

[a] for the classification of each catalyst, see Figure 1.

Table 2 Benchmarking the catalytic activity of Catalyst E against other M-N/C

RSC Advances Accepted Manuscript

catalysts in terms of ORR onset potential, half wave potential and diffusion limiting current in alkaline medium.

Catalyst	E_{onset}/V[a]	$\Delta E_{1/2}$/ V[a]	Diffusion limiting current (mA/cm^2)	Reference
Catalyst E	0.868	0.807	4.1(1600rpm)	This work
Co10-NMCV	0.834	0.774	ca.3.8(1600rpm)	46
3D-CF	0.937	0.794	ca.4.0(1600rpm)	47
FePc/b-MWCNTs	0.938	0.880	3.6(1200rpm)	48
NC-750	0.904	0.744	ca.3(2000rpm)	49

[a] all potentials were converted to the values referred to RHE.

Table 3 Peak area and peak area ratios of the crystal species on the surfaces of catalysts C–G, obtained from XRD results.

RSC Advances Accepted Manuscript

Catalyst[a]	M[b]	M-S[b]	M/M-S
C	0	4232	0
D	0	493	0
E	481	1271	0.38
F	2335	1143	2.04
G	1640	1466	1.12

[a] for the classification of each catalyst, see Figure 1.

[b] M represents metal simple substance, M-S represents metal combined with sulfur.

Table 4 Elemental concentration of catalyst A–G, detected by XPS.

RSC Advances Accepted Manuscript

Catalyst[a]	Metal precursor	C(at.%)	N(at.%)	O(at.%)	S(at.%)	M[b](at.%)
A	$CoSO_4$	89.2	5.15	4.58	0.68	0.38
B	/	96.5	1.59	1.92	/	/
C	$MnSO_4$	95.2	1.49	2.49	0.54	0.31
D	$FeSO_4$	94.6	1.22	3.10	0.56	0.51
E	$CoSO_4$	95.2	1.36	2.59	0.43	0.47
F	$NiSO_4$	95.4	1.79	2.19	0.25	0.35
G	$CuSO_4$	95.2	2.42	1.85	0.31	0.27

[a] for the classification of each catalyst, see Figure 1.

[b] for catalysts A, C, D, E, F and G, M = Co, Mn, Fe, Co, Ni and Cu.

Table 5 Calculated distribution ratio of N through peak assignments of XPS results.

RSC Advances Accepted Manuscript

Catalysts[a]	pyridinic-N	pyrrolic-N	quaternary-N	oxidized-N
A	/	16.9	83.1	/
B	31.1	8.60	41.8	18.5
C	33.2	13.5	49.8	3.60
D	40.9	6.80	47.2	5.10
E	38.6	6.40	53	2.00
F	35.6	11.4	48.7	4.40
G	39.0	5.50	54.3	1.20

[a] for the classification of each catalyst, see Figure 1.

1

RSC Advances Accepted Manuscript